Earth and Space Science

RESEARCH ARTICLE
10.1029/2022EA002277

Simulated Lunar Surface Hydration Measurements Using Multispectral Lidar at 3 μm

D. R. Cremons[1] and **C. I. Honniball**[2]

[1]NASA Goddard Space Flight Center, Greenbelt, MD, USA, [2]NASA Postdoctoral Program, NASA Goddard Space Flight Center, Greenbelt, MD, USA

Key Points:

- We simulated orbital multispectral lidar measurements of the lunar 3 μm hydration feature that could completely characterize the lunar water cycle
- Our simulations included a non-linear mixing model to produce simulated spectra and a least-squares lidar retrieval method to measure the total water abundance
- Using laser wavelengths at 1.5, 2.65, 2.8, and 3.1 μm, the total water abundance was retrieved with a standard deviation 52 ppm or less

Supporting Information:

Supporting Information may be found in the online version of this article.

Correspondence to:

D. R. Cremons,
daniel.cremons@nasa.gov

Citation:

Cremons, D. R., & Honniball, C. I. (2022). Simulated lunar surface hydration measurements using multispectral lidar at 3 μm. *Earth and Space Science*, *9*, e2022EA002277. https://doi.org/10.1029/2022EA002277

Received 9 FEB 2022
Accepted 8 JUL 2022

Author Contributions:

Conceptualization: D. R. Cremons, C. I. Honniball
Data curation: D. R. Cremons
Formal analysis: D. R. Cremons, C. I. Honniball
Investigation: D. R. Cremons
Methodology: D. R. Cremons, C. I. Honniball
Software: D. R. Cremons

Abstract Accurately measuring the variability of spectroscopic signatures of hydration (H_2O + OH) on the illuminated lunar surface at 3 μm as a function of latitude, lunar time of day, and composition is crucial to determining the generation and destruction mechanisms of OH species and understanding the global water cycle. A prime complication in analysis of the spectroscopic feature is the accurate removal of thermal emission, which can modify or even eliminate the hydration feature depending on the data processing methods used and assumptions made. An orbital multispectral lidar, with laser illumination at key diagnostic wavelengths, would provide uniform, zero-phase geometry, complete latitude and time of day coverage from a circular polar orbit, and is agnostic to the thermal state of the surface. We have performed measurement simulations of a four-wavelength multispectral lidar using spectral mixtures of hydrated mid-ocean-ridge basalt (MORB) glasses and lunar regolith endmembers to assess the lidar performance in measuring hydration signatures on the lunar surface. Our results show a feasible system with wavelengths at 1.5 μm, 2.65 μm, 2.8 μm, and 3.1 μm can measure lunar hydration with a precision of 52 ppm (1σ) or better. These results, combined with the uniform measurement capabilities of multispectral lidar make it a valuable spectroscopic technique for elucidating mechanisms of OH/H_2O generation, migration, and destruction.

Plain Language Summary Outstanding questions and conflicting results related to the variability of water and hydroxyl on the lunar surface require new measurement systems and techniques that are ideally independent of the temperature of the surface. A light detection and ranging (lidar) system with multiple laser wavelengths that are sensitive to the total water (H_2O + OH) content of the surface would provide important validation of disagreeing passive results and would fill data gaps at high latitudes on the day side and cover the entire night side. We have performed simulations of a four-wavelength lidar system, which showed the technique is able to measure the amount of total water with a precision of 52 ppm or better. Our results indicate an orbital multi-wavelength lidar would fill crucial data gaps and confirm or refute hypotheses related to the generation mechanisms, form, and migration of water and/or hydroxyl on the surface.

1. Introduction

Hydration on the illuminated lunar surface has now been well established following remote observations of a 3 μm hydration band by five infrared spectrometers (Chauhan et al., 2021; Clark, 2009; Honniball et al., 2020; Pieters et al., 2009; Sunshine et al., 2009). The 2.8–3.5 μm IR hydration feature (hereafter referred to as the 3 μm band) however suffers from uncertainties in removing thermal emission from reflectance measurements made with passive spectrometers (Lucey et al., 2021). The primary complication with interpretation of passive 3 μm band measurements lies in decoupling the radiance contributions of solar reflectance and lunar thermal emission, which are roughly equal near 3 μm at lunar dayside temperatures (Clark, 1979; Vasavada et al., 2012). In addition, the choice of a surface photometric function and the relation of lunar emissivity to reflectance and the applicability of Kirchoff's law further complicate the analysis.

Using data from the Moon Mineralogy Mapper (M^3) spectrometer on the Chandrayaan-1 mission (Green et al., 2011) various analysis methods have been put forward to remove the thermal component. However, interpretations from the same raw M^3 data are not consistent and arrive at conflicting conclusions about the presence and strength of diurnal and latitudinal variations measured by the 3 μm band. Comprehensive summaries and discussion of observations to date in the 3 μm band are given by Grumpe et al. (2019), and Lucey et al. (2021). Here we provide a brief overview. McCord et al. (2011) found strong variations in the 3 μm band depth as a function of latitude and time of day, as well as striking differences between mare and highlands regions. Bandfield

Supervision: D. R. Cremons
Validation: D. R. Cremons
Visualization: D. R. Cremons
Writing – original draft: D. R. Cremons, C. I. Honniball
Writing – review & editing: D. R. Cremons, C. I. Honniball

et al. (2018), found a persistent 3 μm band across the lunar surface, with minimal variations as a function of latitude, time of day, or composition. S. Li and Milliken (2017) found strong variations at low latitudes, asymmetric abundances between morning and evening terminators and little variation at high latitudes. Lastly, Wöhler et al. (2017) and Grumpe et al. (2019) observed no variation below latitude ∼30° and strong symmetric variations above ∼30°. The varying interpretations of observations from a single passive spectrometer makes modeling the behavior of the 3 μm band hard with different models and input parameters being proposed (Farrell et al., 2015; Jones et al., 2018; Tucker et al., 2019). Therefore, passive observations of the 3 μm band are currently not able to constrain the processes that govern the source, retention, or transportation of total water ($OH + H_2O$) measured by the 3 μm band on the lunar surface.

Currently, passive observations of the 3 μm band can only be carried out during the lunar day so there is no information about the behavior of total water on the lunar nightside or within areas of permanent shadow due to the lack of illumination. This leaves large data gaps in constraining the current lunar hydration cycle. Observing the behavior of total water during the lunar night and in permanently shadowed regions (PSRs) is important for understanding the processes governing hydration on the lunar surface and for future exploration and in-situ resource utilization.

In contrast to passive reflectance spectroscopy, active laser (or lidar) reflectance measurements of the lunar surface bypass the need for a natural illumination source and do not require precise knowledge of the temperature or emissivity of the surface. Orbital lidar observations at 3 μm of the lunar surface can be performed regardless of temperature, location, time of day, or illumination conditions (Lucey et al., 2014; Mazarico et al., 2011; Smith et al., 2010). Single-wavelength lidars with lasers emitting at 1.06 μm have identified regions with anomalous albedos at the northern pole of Mercury corresponding to regions of buried and exposed ice (Deutsch et al., 2017) and provided evidence supporting polar surface ice within lunar PSRs (Fisher et al., 2017; Lucey et al., 2014; Zuber et al., 2012). Soon the Lunar Flashlight technology demonstration will carry a multiband reflectometer emitting at four wavelengths between 1 and 2 μm (Cohen et al., 2020) to measure ISRU-relevant quantities of water ice in select regions.

Active reflectance measurements constraining the 3 μm band would provide more conclusive measurements of the diurnal, latitudinal, and compositional variation of the 3 μm hydration signature. These measurements will capture the full diurnal cycle with none of the illumination restrictions of passive approaches. For example, active reflectance observations of strong diurnal and latitudinal trends would support the hypothesis of molecular water moving along temperature gradients on the surface (Hendrix et al., 2019; Honniball et al., 2020; Sunshine et al., 2009). An absent diurnal but strong latitudinal trend would support the hypothesis that the 3 μm band is due to the formation and destruction of metastable hydroxyl from the migration of solar wind hydrogen (Farrell et al., 2015; Starukhina, 2006; Tucker et al., 2019) which has not been shown to cause a temperature-dependent variation in the 3 μm band (McLain et al., 2021; Schaible & Baragiola, 2014). A weak latitudinal trend with hydration present at greater than 50 ppm at all times of day and latitudes would match modeling results for water formation via recombination desorption (Jones et al., 2018). Active reflectance observations will also provide first of its kind measurements of the 3 μm band on the nightside and across the terminators, which would enable discrimination of temperature-dependent migration mechanisms. For example, modeling by Schorghofer et al. (2017) showed that thermally-driven migration of water molecules results in surface concentration peaking around the dawn terminator. This measurement capability would uniquely fill data gaps from current and planned instrumentation and directly address the present ambiguities between hypotheses related to the diurnal and latitudinal variation of the 3 μm band.

We investigated the suitability of this measurement concept by simulating lunar surface reflectance spectra in the lidar (zero-phase) geometry with precisely controlled 3 μm hydration bands. We then use a four-wavelength lidar model to measure the surface hydration using a least-squares spectral unmixing method. We simulated total water ($H_2O + OH$) abundances between 0 and 500 ppm corresponding to the levels measured between 100 and 383 K from recent ground-based observations of the 3 μm band depth on the sunlit surface (Honniball et al., 2020). This range was used to cover possible total water abundances that may be found on the lunar surface, but our spectral measurement results are not dependent on specific diurnal or latitudinal trends.

2. Methods

2.1. Spectral Data Sets

Hydroxyl groups and water molecules exhibit vibrational absorption features near 3 μm associated with the symmetric stretch of the O-H bond. The bonding environment (bond strength and length) determines the precise vibrational frequency at which the absorption occurs. However, the ability to accurately constrain the physical and chemical state of the O-H and speciation (OH vs. H_2O) from the 3 μm feature alone is not clear (Dyar et al., 2010) with the combined OH + H_2O abundance referred to as "total water." Total water may refer to structural OH, OH or H_2O within glasses, adsorbed H_2O, and surficial OH (terminal hydroxyl), all of which exhibit 3 μm absorption bands.

We simulated lunar surface reflectance spectra from 1 to 4 μm under varying levels of hydration by using a Monte Carlo method to generate intimate single scattering albedo mixtures using laboratory reflectance data of Apollo samples from the NASA Reflectance Experiment Laboratory (RELAB) at Brown University and reflectance data from step-wise heating experiments of water-bearing mid-ocean-ridge basalt (MORB) glasses (S. Li, 2016; Shimizu et al., 2016).

We introduced varying levels of hydration to the reflectance simulations using hydrated MORB glass spectra. We chose the hydrated MORB glasses based on their water content range, their visual homogeneity, and having as little alteration as possible (S. Li, 2016). Crucially, the absolute water content was measured independently by secondary-ion mass spectrometry (SIMS) (Shimizu et al., 2016), enabling us to verify the accuracy of our spectroscopic water retrieval. The MORB glasses were heated in a step-wise fashion to remove water allowing for a correlation between the strength of the 3 μm band and water content from SIMS measurements (S. Li & Milliken, 2017). These hydrated MORB glasses have been used to estimate the abundance of water in the lunar 3 μm band of remote sensing datasets (Honniball et al., 2020; S. Li & Milliken, 2017). The Supplementary Material contains spectral comparisons and accompanying discussion of the hydrated MORB glasses used here to the 3 μm band shape from lunar remote sensing data from the InfraRed Telescope Facility (IRTF, Figure S1 in Supporting Information S1) and from M^3 (Figure S2 in Supporting Information S1). The shape of the MORB 3 μm band can also be compared to the hydroxyl feature in laboratory spectra of proton-irradiated Apollo soils (Ichimura et al., 2012; McLain et al., 2021). Ubiquitous (but unquantified) adsorbed surface water is present in the laboratory reference spectra of Apollo samples we used (Figure S3 in Supporting Information S1) due to the high reactivity of lunar soil samples, with similar band shape to the hydrated MORB glasses. Based on these comparisons and its prior use in interpreting lunar remote sensing datasets we believe that the MORB glass spectra represents the best quantitative method of introducing hydration signatures into our spectral mixtures.

In our simulations we separated highlands and mare datasets to test the effects of terrain type on the multispectral reflectance retrieval. For both the highlands and mare datasets, each spectrum was generated from a random mixture of mature and immature Apollo sample spectra, an Apollo pyroxene spectrum, and a MORB spectrum. Representative mature and immature mare sample spectra were selected from Taylor et al. (2001), and mature and immature highlands sample spectra were selected from Taylor et al. (2010). The mature mare sample had 15.7% pyroxene abundance and the immature mare sample had 20.5% pyroxene abundance in the 20–45 μm size fraction (Taylor et al., 2001). The mature highlands sample had 5.1% and pyroxene abundance and the immature highlands sample had 7.4% pyroxene abundance in the 20–45 μm size fraction (Taylor et al., 2010). We also included varying amounts of additional pyroxene in the mixtures to test whether its presence affects the 3 μm band depth determination. Pyroxenes exhibit an absorption band that can extend from 1.4 to 2.6 μm corresponding to a crystal field transition in Fe^{2+} (Burns, 1993; Cloutis, 2002; Sunshine & Pieters, 1993). This broad absorption may coincide with the onset edge of the hydration band, affecting the continuum from which the band depth is determined. The list of Apollo soil samples, spectra labels, and abundance ranges for the mixtures are given in Table 1. The abundance ranges for the glass and overall pyroxene were chosen to mimic the heterogeneity of the lunar surface based on data from Lunar Sourcebook (Table 5.1, Papike et al., 1991).

Finally, we endeavored to test our multispectral lidar retrieval method on a mixture containing a non-MORB glass, also with precisely known water content, to assess how differences in the 3 μm band shape affected the retrieval. For this we used RELAB spectra of orange and yellow synthetic lunar glasses. These glasses have the same bulk chemical composition as green and orange glasses found in Apollo samples. Importantly, the water abundance in the glasses was measured via SIMS by Wetzel and co-authors (Wetzel et al., 2015), which allows

Table 1
Information on Endmember Spectra Used to Generate Intimate Mixtures

Endmember	Sample/Spectrum label	Grain size	Minimum abundance	Maximum abundance
Mature highlands	62231/LR-CMP-098	20–45 μm	0.2	1[a]
Immature highlands	61221/LR-CMP-106	20–45 μm	0.0	0.25
Mature mare	70181/LR-CMP-023	20–44 μm	0.2	1[a]
Immature mare	71061/LR-CMP-026	20–44 μm	0.0	0.25
Pyroxene	15555/LR-CMP-168	0–125 μm	0.0	0.25
Hydrated glass	MORB D38A	63–75 μm	0.0	0.3
Synthetic lunar orange glass	OGV-5/RM-REM-140-A	0–45 μm	0.0	0.3
Synthetic lunar yellow glass	YG-5/RM-REM-139-A	0–45 μm	0.0	0.3

Note. The main simulations used mixtures of the top six endmembers. Additional limited simulations were performed using the synthetic lunar glasses.
[a]Amounts were determined last to ensure the endmember abundances summed to 1 for each mixture.

us to use it to create spectral mixtures with a known total water amount. The orange synthetic lunar glass had a total water content of 390 ppm, and the yellow synthetic lunar glass had a total water content of 305 ppm as measured by SIMS.

2.2. Removal of Terrestrial Water Signature From Endmember Spectra

The Apollo soil spectra from the RELAB database all exhibited various absorption features between 2.6 and 4 μm indicating the presence of unquantified hydration and organic doublets near 3.5 μm, both likely from a terrestrial source. Our goal was to introduce only a quantified hydration signature to compare with the retrieved value, which meant we must first remove this unknown signature from the endmember spectra. We performed a linear fit of the reflectance data for the five Apollo samples using anchor points at 2.6 and 4.0 μm, then substituted the linear fit into the endmember spectrum to remove the absorption feature (Figure S3 in Supporting Information S1). This is analogous to the lunar continuum removal process used to isolate and determine the 3 μm band depth of spectra from the EPOXI instrument on Deep Impact (Sunshine et al., 2009). Finally, the endmember spectra were interpolated to a uniform 5-nm spectral sampling from 1 to 4 μm. The reflectance spectra of the endmembers are shown in Figure 1.

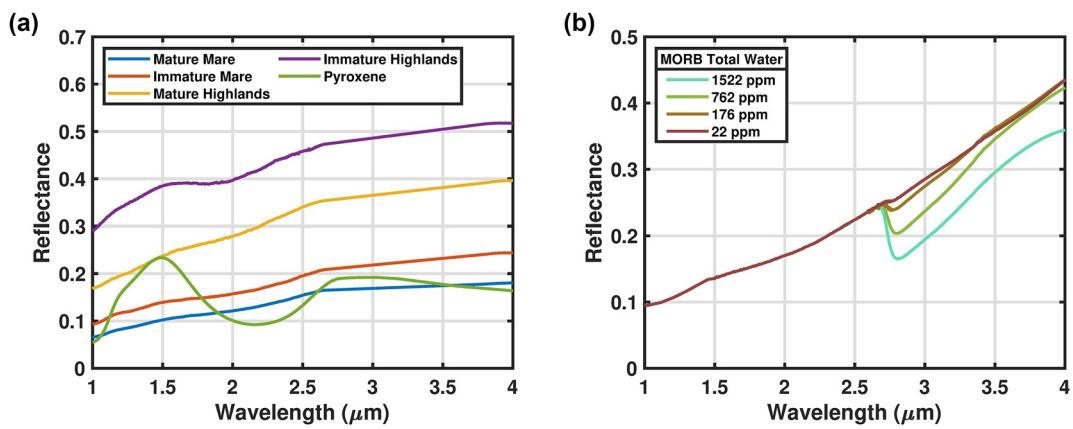

Figure 1. Processed endmember laboratory reflectance spectra. Each spectrum was processed to remove hydration and organic contamination features as described in the text. (a) Regolith and pyroxene spectra as described in Table 1. (b) Laboratory MORB glass reflectance spectra used to simulate surface hydration in the reflectance simulations. The raw MORB spectra were normalized to each other at a wavelength 2.6 μm.

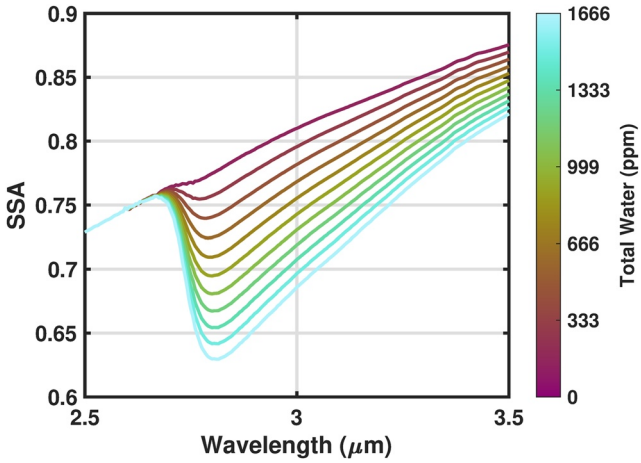

Figure 2. A Subset of interpolated MORB single scattering albedo spectra. The interpolated spectra correspond to total water values of (from low to high): 0, 150, 300, 450, 600, 750, 900, 1,050, 1,200 ppm, and 1,350, and 1,500 ppm.

2.3. Interpolation of MORB Glass Spectra

We used four MORB glass spectra with SIMS-measured water content of 1,522, 762, 176, and 22 ppm (Figure 1b). All four spectra were obtained after heating to 600°C or above, which ensured the removal of surface-bound water (Dyar et al., 2010). Our simulated total water range was 0–500 ppm, with glass abundances between 0 and 0.3. Thus, finer resolution steps in hydration were needed compared to the experimental step-heating spectra. We generated synthetic MORB glass spectra at steps of 1 ppm total water from 0 to 1,666 ppm via linear interpolation of the step-heating data. At each wavelength from 2.65 to 4 μm, the SSA values for each of the four experimental spectra were used to calculate the effective single-particle absorption thickness (ESPAT) value (1-SSA/SSA) for that wavelength. The ESPAT values at each wavelength were fit linearly using the total water abundance as the independent variable (Figure S7 in Supporting Information S1). This gave us an analytical expression with total water abundance as the input and SSA as a function of wavelength as the output enabling us to create MORB glass SSA spectra with a near-continuous range of water content, which we used to precisely introduce hydration to the overall spectral mixture. A subset of the interpolated MORB glass spectra is shown in Figure 2.

We used these interpolated MORB glass spectra to vary the total water abundance in our simulations. In each mixture both the amount of glass in the mixture (ranging from 0 to 0.3) as well as the amount of hydration in the glass (ranging from 0 to 1,666 ppm) were randomly varied via a Monte Carlo method. The overall range of input total water in the simulations was 0–500 ppm, which covers the range of lunar total water ranges observed remotely with the IRTF by Honniball et al. (2020) and is within the range observed with M^3 by S. Li and Milliken (2017).

2.4. Spectral Mixing and Reflectance Spectrum Generation

One thousand mare spectral mixtures and 1,000 highlands spectral mixtures were generated using a Monte Carlo method based on the endmember fractional ranges given in Table 1. We used a Monte Carlo method to assess the accuracy of the multispectral lidar method as they enabled us to test a wider range of spectral shapes and assess the effects of the measurement SNR and pyroxene abundance. To create the spectral mixtures, each endmember reflectance spectrum was first converted to single-scattering albedo (SSA) using the methods of Hapke (2012) and least-squares minimization. The reflectance of the endmember spectra measured in the laboratory (which Hapke calls the radiance coefficient, but will be referred to as reflectance here) is related to the SSA in the Hapke model by (Lucey, 1998):

$$R = \frac{\omega}{4}\frac{\mu_0}{(\mu+\mu_0)}\{(1+B)P + H(\omega)H_0(\omega) - 1\} \quad (1)$$

where R is the bidirectional reflectance, ω is the SSA, and μ and μ_0 are the cosines of the emission and incident angles, respectively. P is the scattering phase function which we set at 0.15 for anisotropic scattering based on the modeled mean particle phase function for lunar soil (Goguen et al., 2010). H and H_0 are the Ambartsumian-Chandrasekhar H function, which we computed the H functions using the approximation from equation 8.57 from Hapke (2012). B is the backscattering function which describes the opposition effect (Hapke, 1986) and is approximated by:

$$B = \frac{1}{1+\left(\frac{1}{h}\right)tan\left(\frac{g}{2}\right)} \quad (2)$$

where g is the phase angle and h is the angular width parameter and can be described by:

$$h = -\frac{3}{8}ln(1-\phi) \quad (3)$$

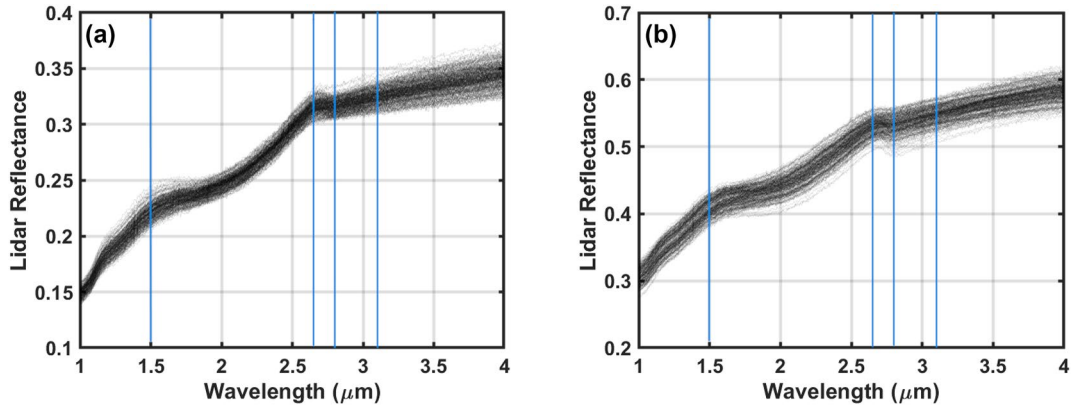

Figure 3. Subset of lidar reflectance spectra (zero-phase reflectance) using the spectral mixing methods described here. Each frame shows 200 individual spectra. (a) Spectra using mare endmembers. (b) Spectra using highlands endmembers. The blue lines denote the lidar wavelengths chosen for this study.

where ϕ is the filling factor and set to 0.41 for the lunar regolith (Bowell et al., 1989). All the endmember spectra were measured with a viewing geometry of $\mu = 0$, $\mu_0 = 30$, and $g = 30$.

We then mixed the endmember SSA spectra using randomized mass fractions within the bounds described in Table 1 to simulate an intimate mixture of particles and determine the average SSA:

$$\omega_{Ave} = \frac{\sum_i \frac{M_i \omega_i}{\rho_i d_i}}{\sum_i \frac{M_i}{\rho_i d_i}} \tag{4}$$

where i denotes the ith endmember, M_i is the mass fraction, ω_i is the endmember SSA, ρ_i is the endmember density, and d_i is the endmember mean grain diameter. For each spectral endmember, we used the average value of the grain size range listed in the RELAB database, which can be found in Table 1. We used a density of 1.8 g/cm^3 for the highlands and mare regolith (McKay et al., 1991), a density of 3.2 g/cm^3 for the pyroxene (Chai et al., 1997), and a density of 2.8 g/cm^3 for the MORB glass (Almeev et al., 2008). Once the average SSA was determined at each wavelength, we used the Hapke radiative transfer model in an inverse fashion to generate bidirectional reflectance spectra of the mixtures at zero phase to simulate the lidar reflectance. With this change in viewing geometry, we modified the scattering phase function, P, to 1.5 based on models of lunar surface scattering properties (Goguen et al., 2010) and normal albedo measurements of mare and highlands regions from the lunar orbiter laser altimeter (LOLA) (Lucey et al., 2014). A subset of 200 of the 2,000 total spectral mixtures are shown in Figure 3.

2.5. Lidar Wavelengths and Simulated Measurement Error

Passive spectrometers have difficulties with removal of the thermal emission signature and accounting for effects of observation geometry near the terminators that may introduce error in the total water abundance measurement, even with continuous spectral sampling. The benefits of an active reflectance measurement, mainly the fixed, zero-phase viewing geometry and ability to remove the effects of surface temperature, necessitate a spectral illumination source. Wideband illumination sources such as tungsten filament lamps and supercontinuum lasers may be suitable for short-range measurements (tens of meters), but orbital measurements will need to rely on discrete laser wavelengths to achieve a suitable signal-to-noise ratio at a realistic mass and power. Surface reflectance from a lidar is determined by measuring the transmitted laser energy, return laser energy, and range to the target along with fixed instrument parameters (see the Supporting Information for further details). Determining the total water abundance from the 3 μm band has generally been done using the ESPAT function, which relates the single scattering albedo at the band minimum and lunar continuum to the total water abundance for a given grain size (Hapke, 2012; Honniball et al., 2020; S. Li & Milliken, 2017). In the ESPAT method, the wavelengths that define the continuum and band minimum are not fixed but are chosen based on a convex-hull method.

We chose four lidar wavelengths at which to measure the zero-phase surface reflectance, distributing the wavelengths based on our desire to constrain the 3 μm band depth and shape. We selected lidar wavelengths at 1.50 μm, 2.65 μm, 2.80 μm, and 3.10 μm. The wavelengths at 1.50 and 2.65 μm constrain the lunar continuum, while those at 2.80 and 3.10 μm constrain the OH band depth and shape to enable a more accurate retrieval of the total water content. By rationing the two wavelengths within the absorption band we can determine where the deepest portion of the band lies. From Figure 1, the band minimum of the hydroxyl absorption occurs at 2.80 μm and thus offers the highest contrast between the 3 μm total water feature and the lunar continuum. Although this work is aimed at total water signatures across the lunar surface, these wavelengths would also offer high reflectance contrast in polar regions with surface water ice, for which the highest k-value (imaginary component of the index of refraction) occurs at 3.10 μm (Warren & Brandt, 2008). We note these are not necessarily the only viable wavelengths for measuring surface hydration with a multispectral lidar, and we intend to study the optimization of these wavelengths in the future. Upcoming missions to the lunar surface will perform chemical, spectroscopic, and mineralogical studies to increase our knowledge of the form and content of lunar hydration that will all help to refine the number and placement of multispectral lidar wavelengths.

The reflectance measurement precision at each lidar wavelength depends on the ability to accurately measure the transmitted laser pulse energy and the return pulse energy from the lidar. From these measurements (and the range to the surface) the lidar equation is used to retrieve the surface reflectance (Cohen et al., 2020; Lucey et al., 2014; Sun, 2017). The contribution of signal from thermal emission and solar reflectance was assumed to be removed using the continuous signal that is present between laser pulses when no laser illumination is present. For these simulations we developed a multispectral lidar performance model (see supplementary material) to determine a realistic signal-to-noise ratio with which reflectance uncertainty can be added to the synthetic spectra. From our model, we conservatively estimated an SNR of 250 for each lidar wavelength under sunlit conditions from a 50 km orbit with a 25-cm diameter receiver telescope, 100 μJ output pulse energy per wavelength, and assuming a 1-s integration time (Figure S11 in Supporting Information S1). The laser and detector performance have been demonstrated for this wavelength regime using optical parametric oscillator-based lasers (Cremons et al., 2020; S. X. Li et al., 2017), and a sensitive HgCdTe APD detector (Abshire et al., 2018; Hubbs et al., 2018; Sun et al., 2019). We do not intend to limit the lidar system or subsystem architecture here, but to ensure the simulations include reasonable measurement conditions for an orbital multispectral lidar. The results section includes simulations of total water retrieval error as a function of measurement SNR, as well as the effect of differing lighting conditions on instrument performance.

We simulated the lidar measurement precision by adding randomly distributed Gaussian noise to the reflectance spectra. The noise was zero-mean with a variance equal to the noiseless reflectance divided by the SNR. We justify the assumption of zero-mean noise because the sources of bias (the detector dark noise and solar/thermal background photons) are measured between laser pulses and removed from the return pulse energy measurement. Reflectance spectra in the lidar geometry for mixtures using mare and highlands soils with noise added are shown in Figure 3. A total of 1,000 mare spectra and 1,000 highlands spectra were generated using the methods described above.

2.6. Spectral Unmixing Using Non-Negative Linear Regression

We used a non-negative linear least-squares algorithm to solve for the total water abundance from the four lidar measurements of the noisy reflectance spectra. Our method is based on those of Mustard and Pieters (1987), and S. Li and Li (2011), who applied a linear-least squares algorithm on reflectance spectra to retrieve mineral endmember abundances. For an intimate mixture as we have modeled here, the abundance of each endmember is non-linear in reflectance, so the four reflectance values at the lidar wavelengths were first converted back to SSA using the Hapke model of radiative transfer with the parameters given above. We used four endmember spectra to solve for each four-wavelength spectrum. Two of the four endmembers were from the MORB glass step-heating experiment: the 1,522 ppm and 22 ppm experimental spectra (Figure 1b). The 1,522 and 22 ppm spectra were chosen as they represent the two extremes of the 3 μm band shapes in the mixtures. The other two endmembers were the mature mare spectrum (70181/LR-CMP-023), and the immature highlands (61221/LRCMP-106). These regolith spectra were chosen because they represent the extrema with respect to the highest and lowest spectral slopes for the lunar continuum (Figure 1a). The same four endmember spectra were used for all simulations.

The system of linear equations to be solved is given by:

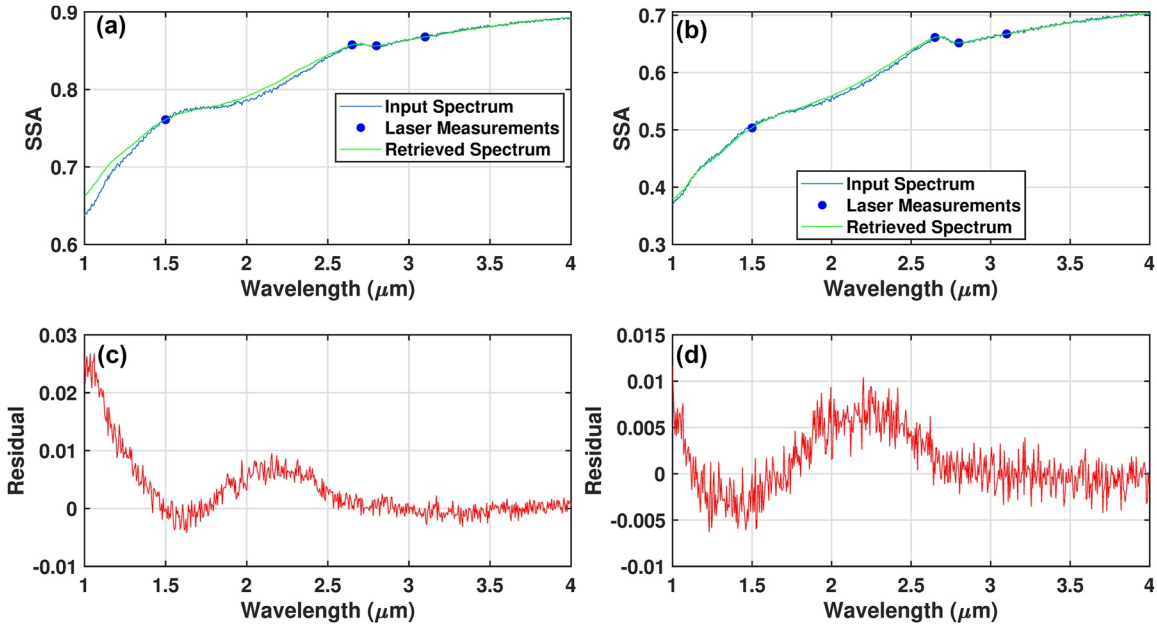

Figure 4. Representative results of spectral unmixing using least-squares regression. (a) The input spectrum is from the highlands simulations. (b) The input spectrum is from the mare simulations. The green line is the retrieved spectrum generated by multiplying the retrieved endmember abundances by the endmember SSAs. Only the reflectance values at the four blue points were used in the retrieval process. (c) and (d) Residuals from the spectral unmixing results determined by subtracting the mixture SSA spectrum (calculated from the noisy reflectance spectrum) from the retrieved spectrum in (a) and (b), respectively.

$$\begin{bmatrix} SSA_{\lambda 1M} & SSA_{\lambda 2M} & SSA_{\lambda 3M} & SSA_{\lambda 4M} \end{bmatrix} = \begin{bmatrix} SSA_{C1,\lambda 1} & SSA_{C2,\lambda 1} & SSA_{C3,\lambda 1} & SSA_{C4,\lambda 1} \\ SSA_{C1,\lambda 2} & SSA_{C2,\lambda 2} & SSA_{C3,\lambda 2} & SSA_{C4,\lambda 2} \\ SSA_{C1,\lambda 3} & SSA_{C2,\lambda 1} & SSA_{C3,\lambda 3} & SSA_{C4,\lambda 3} \\ SSA_{C1,\lambda 4} & SSA_{C2,\lambda 1} & SSA_{C3,\lambda 4} & SSA_{C4,\lambda 4} \end{bmatrix} \begin{bmatrix} A_{C1} \\ A_{C2} \\ A_{C3} \\ A_{C4} \end{bmatrix} \quad (5)$$

where SSA λ_{iM} is the single-scattering albedo at the *ith* wavelength from the noisy spectrum, $SSA_{Cj,\lambda i}$ is the SSA of the *jth* endmember at the *ith* wavelength, and A_{Cj} is the abundance of the *jth* endmember. Following the least-squares fitting, the retrieved abundances of the MORB endmembers were multiplied by the total water in each endmember (i.e., 1,522 ppm and 22 ppm). This resulted in a measured total water abundance for each spectrum, which was then compared to the input total water abundance for each mixture.

3. Results

3.1. Representative Spectral Unmixing Results and Total Water Retrievals

Figure 4 shows the results of the spectral unmixing technique described above for two of the 2,000 simulated spectra. We remind the reader that the four lidar SSA values denoted by the blue dots in Figures 4a and 4b were the only values used to solve for the abundances of each of the endmember spectra. Multiplying the lidar-derived endmember abundances by their respective SSA spectra gives the green spectra in Figure 4. As expected, the least squares algorithm minimizes the residual SSA near the lidar wavelengths. This can be seen in the residual spectrum (Figures 4c and 4d) generated by subtracting the noisy simulated spectrum from the retrieved spectrum. The lowest residuals are near the measurement wavelengths. Error in the total water abundance retrieval is visible from the small absorption feature in the residual spectra near 2.8 μm.

The results showing the derived and input abundances for the spectra in Figure 4 are shown in Table 2. This highlands simulation had a randomly chosen input glass fraction of 0.27 and a randomly selected interpolated MORB

Table 2
Summary of Spectral Unmixing Results for the Spectra in Figure 4

	Highlands simulation		Mare simulation	
Endmember	Input abundance	Least-squares abundance	Input abundance	Least-squares abundance
Glass Abundance (Interpolated Hydration Spectrum)	0.27 (581 ppm spectrum)	0.06 (1,522 ppm endmember) 0.12 (22 ppm endmember)	0.25 (1,548 ppm)	0.17 (1,522 ppm endmember) 0.03 (22 ppm endmember)
Mature mare	0	0.15	0.48	0.40
Immature mare	0	Not retrieved	0.20	Not retrieved
Mature highlands	0.40	Not retrieved	0	Not retrieved
Immature highlands	0.18	0.31	0	0.03
Pyroxene	0.15	Not retrieved	0.06	Not retrieved
Total Water Abundance	156 ppm	119 ppm	390 ppm	309 ppm
Total Water Error	**−37 ppm**		**−81 ppm**	

Note. The input glass abundance and interpolated hydration spectrum (see Figure 2) were independently and randomly selected for each simulation.

spectrum with 581 ppm total water (0.27 × 581 ppm = 156 ppm input abundance). The least-squares algorithm was tasked with fitting this spectral mixture using the two MORB endmember spectra (1,522 ppm and 22 ppm), as well as the mature mare spectrum and immature highlands spectrum. The line shape of the input MORB spectrum (581 ppm) is about 1/3 of the way between the two endmembers (22 and 1,522 ppm), and the least-squares algorithm resulted in a 1:2 mixture of the two MORB endmembers (0.06 of the 1,522 ppm endmember and 0.12 of the 22 ppm endmember). The total water error for this example, defined as the measured total water abundance minus the input total water abundance was −37 ppm.

The mare simulation had a glass fraction of 0.25 and an interpolated MORB spectrum selection with 1,548 ppm total water. Here, the least-squares algorithm mixed in much more of the high-water content MORB spectrum, as 1,548 ppm is closer to 1,522 than it is to 22 ppm, and the shape of the 3 μm feature was better fit with the closest endmember. For the mare simulation here, the total water error was −81 ppm.

The abundances of the other endmembers (regolith spectra and pyroxene) were not retrieved with high accuracy, though this is expected based on the placement of the lidar wavelengths and the similar spectral shape of the regolith endmembers. The regolith spectra are primarily used to fit the overall spectral magnitude (the continuum albedo) and the continuum spectral slope. Similarly, there is no constraint on the abundances summing to 1, such that a low abundance of immature mare and a high abundance of mature mare may appear equally valid to the least-squares algorithm based on their spectral similarity. However, the least-squares algorithm was able to correctly identify the soil as primarily mare or highlands in nature.

3.2. Total Water Retrieval as a Function of Temperature for Mare Mixtures

The total water retrieval results for the mare mixtures are shown in Figure 5. Input abundance is defined above as the glass fraction multiplied by the total water abundance in the randomly chosen synthetic MORB spectrum. Retrieved total water was calculated from the least-squares endmember abundances using the following formula:

$$A_{T.W.}[ppm] = (A_{1522} \cdot 1522) + (A_{22} \cdot 22) \quad (6)$$

where $A_{T.W.}$ is the retrieved total water abundance in parts per million, A_{1522} is the least-squares abundance of the 1,522 ppm MORB endmember, and A_{22} is the least-squares abundance of the 22 ppm MORB endmember. The mare multispectral lidar simulations exhibited a mean error of −38 ppm and a standard deviation of 52 ppm. This mean error represents a deviation from the desired one-to-one relationship between input abundance and retrieved abundance and a statistical underestimation of the total water content. The root mean square error (RMSE) for the mare simulations was 65 ppm. Figure 5b shows a histogram of the total water error, defined as the retrieved total water minus the input total water. The mean error can be observed by the peak in the histogram at a value slightly less than 0 ppm total water error.

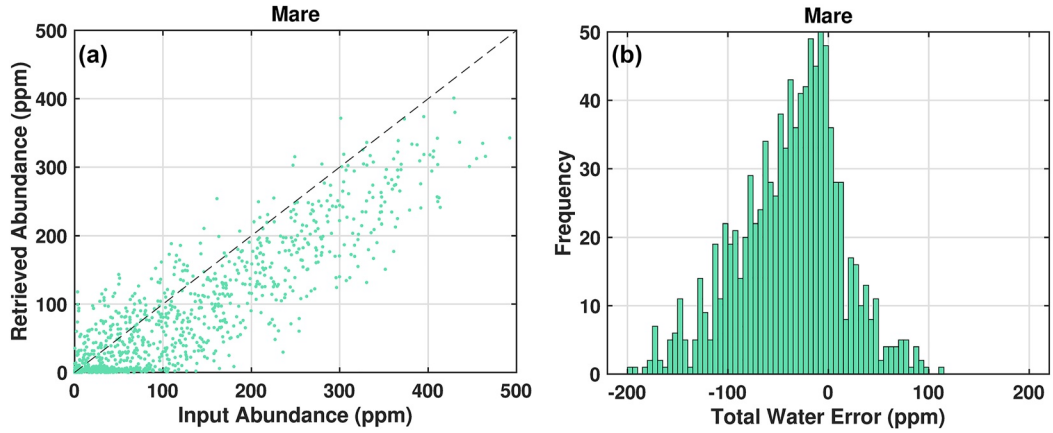

Figure 5. (a) Results for all 1000 mare simulations. Each dot denotes a single retrieval. The black dotted line denotes a slope of 1. (b) Histogram of total water error. The histogram bin width is 5 ppm.

3.3. Total Water Retrieval as a Function of Temperature for Highlands Mixtures

The results for the highlands simulations are shown in Figure 6 using the same conventions as Figure 5. In general, the highlands results were similar to the mare simulations, though slightly more accurate. The mean error and standard deviation were −39 and 38 ppm, respectively. The RMSE of the highlands simulations was 55 ppm compared to 65 ppm for the mare simulations. The statistics for the mare and highlands simulations are given in Table 3.

3.4. Effects of SNR on Total Water Error

We tested a range of SNR values for the entire set of simulated spectra (1,000 mare and 1,000 highlands spectra) to quantify the standard deviation of the retrieval under different noise conditions. These simulations were run using the same spectral mixtures as the data presented in Figures 5 and 6, with the only difference being the noise-addition process. For each SNR, noisy-spectra were re-generated from the mixture SSA spectra using different magnitudes for the Gaussian-distributed reflectance error. We then performed the total water retrievals in the same manner as the prior simulations. The standard deviations for the range of SNRs tested are given in Table 4. Figure 7 shows a graphical representation of the total water error standard deviation as a function of SNR. The standard deviation decreased as a function of increasing SNR following a power-law curve with an exponent of −0.37 for the mare simulations and −0.34 for the highland simulations. In an ideal case where

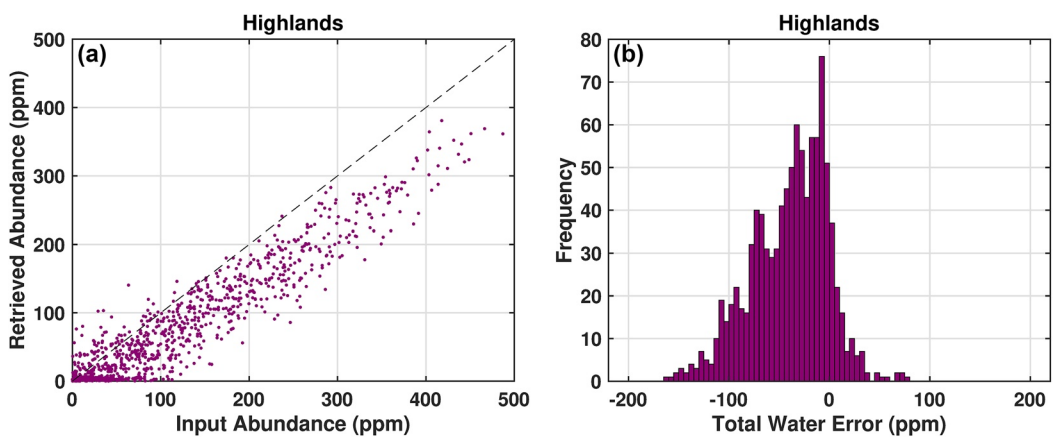

Figure 6. (a) Results for all 1,000 highlands simulations following the conventions of Figure 5. (b) Histogram of total water error following the conventions of Figure 5.

Table 3
Summary of Total Water Retrieval Results for Mare and Highlands Simulations

Mixture type	Total water mean error	Total water error standard deviation	Total water RMSE
Mare	−38 ppm	52 ppm	65 ppm
Highlands	−39 ppm	38 ppm	55 ppm

the total water abundance error was only due to random error in the band depth measurement, the exponent is expected to be −0.5 (Gardner, 1982) (see Equation S1 in Supporting Information S1).

We hypothesize these slightly lower exponents are due to the correlated nature of the four reflectance measurements in determining the total water abundance, such that errors in any one measurement (either the baseline or the 3 μm band) will negatively affect the other wavelength measurements. Not all four wavelengths are expected to affect the error uniformly; we expect that errors in the 2.65 and 2.8 μm measurements affect the total water error more than the 1.5 and 3.1 μm measurements, though further simulations are needed to test this sensitivity, along with the sensitivity to the precise laser wavelengths themselves. Overall, the performance as a function of SNR followed the expected power law behavior and suggests that engineering efforts to increase the measurement SNR beyond ∼300 will have diminishing returns on reducing the overall measurement uncertainty.

The relationship between SNR and retrieval precision is also useful for estimating the performance under night or shadowed conditions. From the SNR model results shown in Figure S11 in Supporting Information S1, the shadowed terrain SNR for this design is >300 at all lidar wavelengths. From the equations shown in Figure 7, this corresponds to slight improved performance with a standard deviation of 38 ppm for the Highlands case and 48 ppm for the Mare case. Thus, the performance of this instrument will depend more strongly on the absolute regolith reflectance than on the illumination state of the surface, as detector dark noise, not reflected solar light, is the limiting noise source.

3.5. Effects of Pyroxene on Retrievals and Band Depth

We chose to add between 0% and 25% of pyroxene to the spectral mixtures to test the effects of pyroxene abundance on the multispectral lidar total water retrieval. This includes determining whether the larger error observed in the mare mixtures was related to the higher pyroxene abundance in the mare mixtures. For our simulations the pyroxene abundance had a small effect on the errors in the retrieval. In general, the total water error became more negative (i.e., the underestimation of total water was greater) in a linear fashion as pyroxene abundance went up, though it was a minor effect. The magnitude of the effect was 0.6 ppm per percent pyroxene. The effect of pyroxene was more pronounced in trials where the continuum lidar wavelength was shifted shorter in wavelength toward the 2 μm pyroxene band. We performed a second set of lidar retrievals on the 2,000 simulated spectra using a 2.5 μm lidar wavelength instead of 2.65 μm and observed the overall total water abundance accuracy and precision went down and a stronger pyroxene trend was observed (−2 ppm per percent pyroxene).

To explore the impact of this effect on band depth in general (not specific to the four-wavelength lidar retrievals) we created new spectral mixtures using the methods of Sections 2.4 through 2.6 with a fixed amount of MORB glass (0.3) and a fixed interpolated MORB spectrum (1,000 ppm), but randomly varied amounts of pyroxene and regolith spectra. Our intent was to isolate the effect of pyroxene abundance on the band depth for both mare and highlands terrain. We then processed the lidar reflectance spectra to determine the 3 μm band depth. Here we define band depth for the lidar as the difference between a linear continuum with anchor points at 2.5 or 2.65 and 3.5 μm and the measured reflectance at 2.8 μm. This ensures a band depth of zero when no hydration is present based on our method of using a linear fit to remove terrestrial water from the endmember spectra. This band depth was calculated for the 2,000 new spectral mixtures (Figure 8). We observed clear linear trends of measured band depth as pyroxene abundance increased, however, the slope of the trend changed depending on where the continuum was anchored. When 2.5 μm was used as a continuum reference, the band depth decreased as a function of increasing pyroxene abundance as the 2 μm pyroxene band edge pulled down the continuum reflectance. Using 2.65 μm as a continuum anchor, the band depth increased with pyroxene abundance as the local maximum in the pyroxene spectrum raised the continuum reflectance.

Table 4
Summary of Total Water Retrieval Results at Various SNRs for a Subset (200) of the Spectral Mixtures

SNR	Mare total water error standard deviation	Highlands total water error standard deviation
10	170	122
50	100	63
100	63	50
250	52	38
500	40	35
1000	38	32

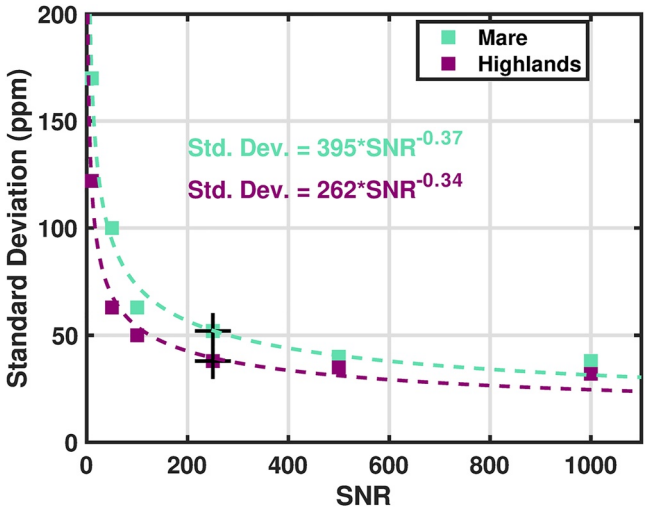

Figure 7. Total water standard deviation as a function of SNR. The purple squares denote the standard deviations from the highlands simulations and the green squares denote the standard deviations from the mare simulations. The black crosses denote the values for the histograms and scatter plots in the prior sections for SNR = 250. The dotted lines are best-fit power laws with the formulae shown.

For both continuum wavelengths the highlands simulations showed a larger effect of pyroxene abundance on band depth, which aligns with previous studies showing the OH band depth is greater in brighter host material (Starukhina & Shkuratov, 2010). A similar linear trend to what we observe in our simulations was reported by McCord et al. (2011), who compared the 2 μm pyroxene and 2.8 μm hydration band depths from M^3 observations. They cautioned the strength of the correlation is dependent on how the band strengths are measured and continua defined, which our simulation results here reinforce.

We conclude band depth effects due to pyroxene shown in Figure 8 are due to two effects. First, the spectral collocation of the OH absorption feature and the local reflectance maximum of the pyroxene (see Figure 1a) decreases (i.e., fills in) the 3 μm band. Second, the 2 μm pyroxene absorption modifies the lunar continuum used to compute the band depth from which the total water abundance is calculated. We chose 1.5 and 2.65 μm as the continuum lidar wavelengths to purposely avoid the pyroxene crystal field transition near 2 μm and its effects on the continuum fit. We note these effects are relevant not only for multispectral lidar measurements but also for measurements of the 3 μm band depth and continuum using passive methods. Careful laboratory reflectance studies of the 3 μm hydration band in pyroxene-bearing mixtures would be valuable in interpreting current and future remote sensing datasets.

3.6. Synthetic Lunar Glass Mixture Results

The hydrated synthetic lunar glass mixtures (1,000 of both orange and yellow glass) were generated in the same way as the mixtures using MORB glass, including the abundance ranges, other endmembers (regolith and pyroxene), and radiative transfer methods. The only difference was that the amount of water in the synthetic glasses was constant and only the glass abundance was used to vary the total water amount in the mixture. The retrievals were also conducted in the same fashion as the MORB mixtures, including the measurement SNR (250), four lidar wavelengths, and the four endmember spectra used in the least-squares algorithm: the 1,522 ppm and 22 ppm MORB glass spectra, immature mare spectrum, and mature highlands spectrum. The results of the synthetic lunar glass simulations are shown in Figure 9.

The synthetic glass mixture results show that the multispectral lidar retrieval method using the two experimental MORB endmember spectra to fit the 3 μm feature performs similarly for the interpolated MORB glass and

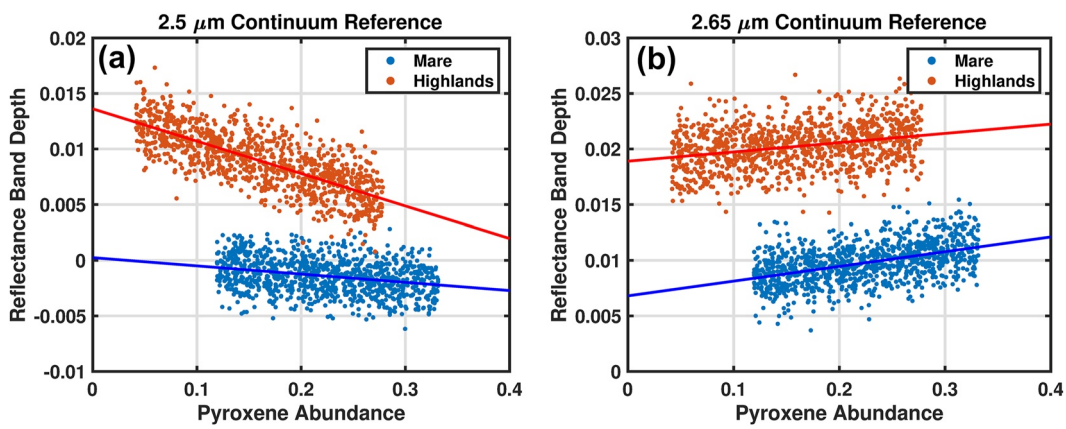

Figure 8. Band depth at 2.8 μm as a function of pyroxene abundance (pyroxene in regolith endmembers + added pyroxene in mixture) using different continuum wavelengths. Every mixture shown here contained 300 ppm total water abundance. Random noise was added to each spectrum to simulate the multispectral lidar SNR. Each point corresponds to a separate spectrum and the solid lines denote a linear fit to the data.

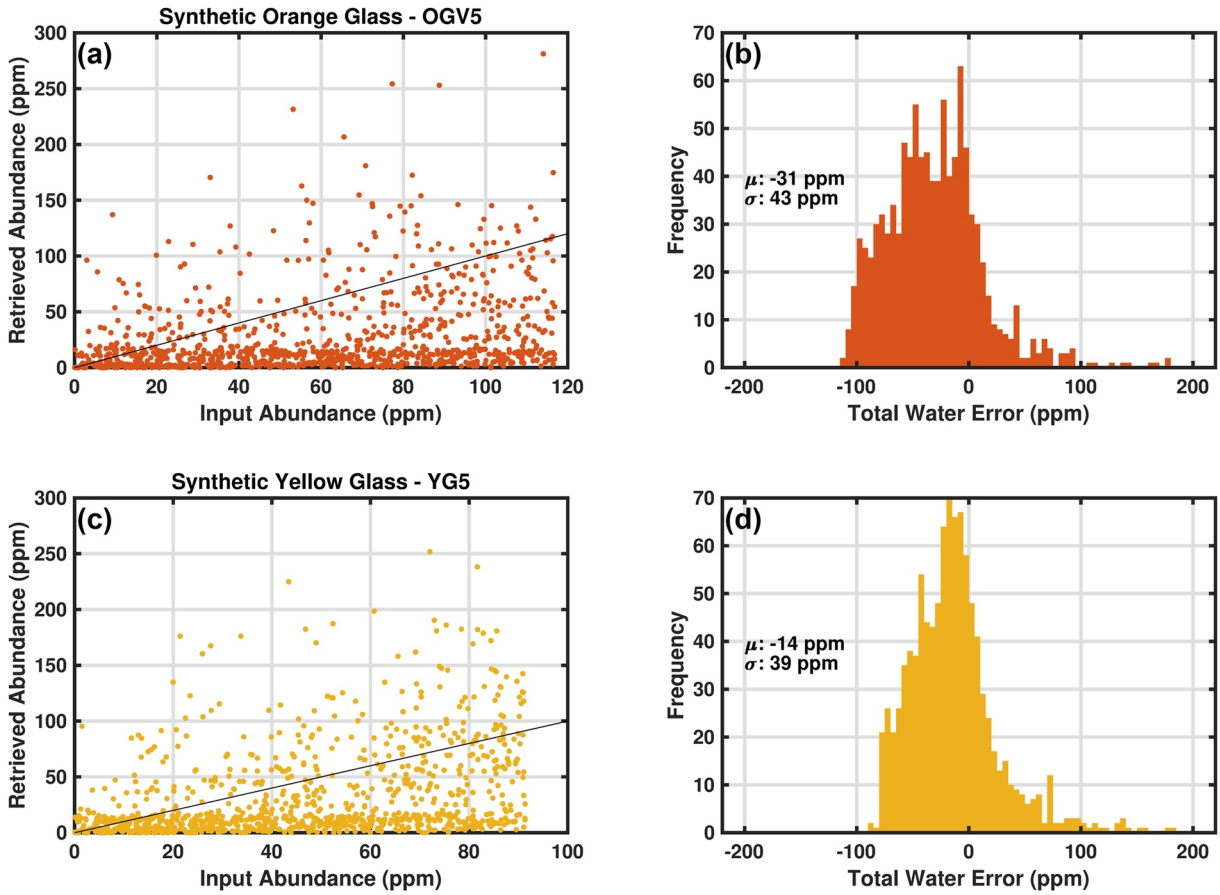

Figure 9. Synthetic lunar glass mixture retrieval results. (a) Retrieved total water abundance as a function of input total water abundance for mixtures including synthetic orange glass following the conventions of Figures 5 and 6. (b) Histogram of total water error for the synthetic orange glass simulations. μ denotes the mean error and σ denotes the standard deviation for the simulations. (c) Retrieval results for the synthetic yellow glass mixtures following the conventions of (a). (d) Histogram of total water error for the synthetic yellow glass mixtures.

synthetic glass mixtures. Both glass mixtures had a negative mean error, with the orange glass mean error (−31 ppm) being closer to the MORB results (−38 ppm) given in Table 3, and the yellow glass mean error (−14 ppm) being lower than the MORB results. The standard deviation for the glass mixture retrievals were very close to one another and the MORB results.

4. Discussion

The highlands simulations exhibited a lower standard deviation for the total water error than the mare simulations, and this trend held over the entire range of SNRs tested. The higher total water sensitivity for highlands spectra is a direct consequence of the non-linearity of mixing single scattering albedos. A brighter surface host material (highlands) manifests a stronger absolute reflectance band depth for a given total water abundance than darker surface material (mare). This effect was similarly demonstrated by Starukhina and Shkuratov (2010) in their 3 μm band modeling efforts related to theories of solar wind proton implantation. McCord et al. (2011) also identified a trend in their M^3 data of stronger 3 μm absorptions in more feldspathic material, however, it is not clear whether this is a chemical/mineralogical effect or an optical effect of the higher albedo of highlands regions, as observed here. We demonstrate this effect in Figure 10, where a subset of the highlands and mare simulations with the same total water abundance exhibit differing band depths. All the spectral mixtures shown in Figure 10 have a total water abundance between 245 and 255 ppm, for which the band depth may be expected to be constant. However, the highlands spectra have a clearly stronger 3 μm band (Figure 10b), demonstrating this albedo effect (Lucey et al., 2021). Because of the non-linearity of reflectance with respect to SSA, this effect is not present in SSA (Figure 10c). Since the retrieval error arises from band depth measurement error, a stronger

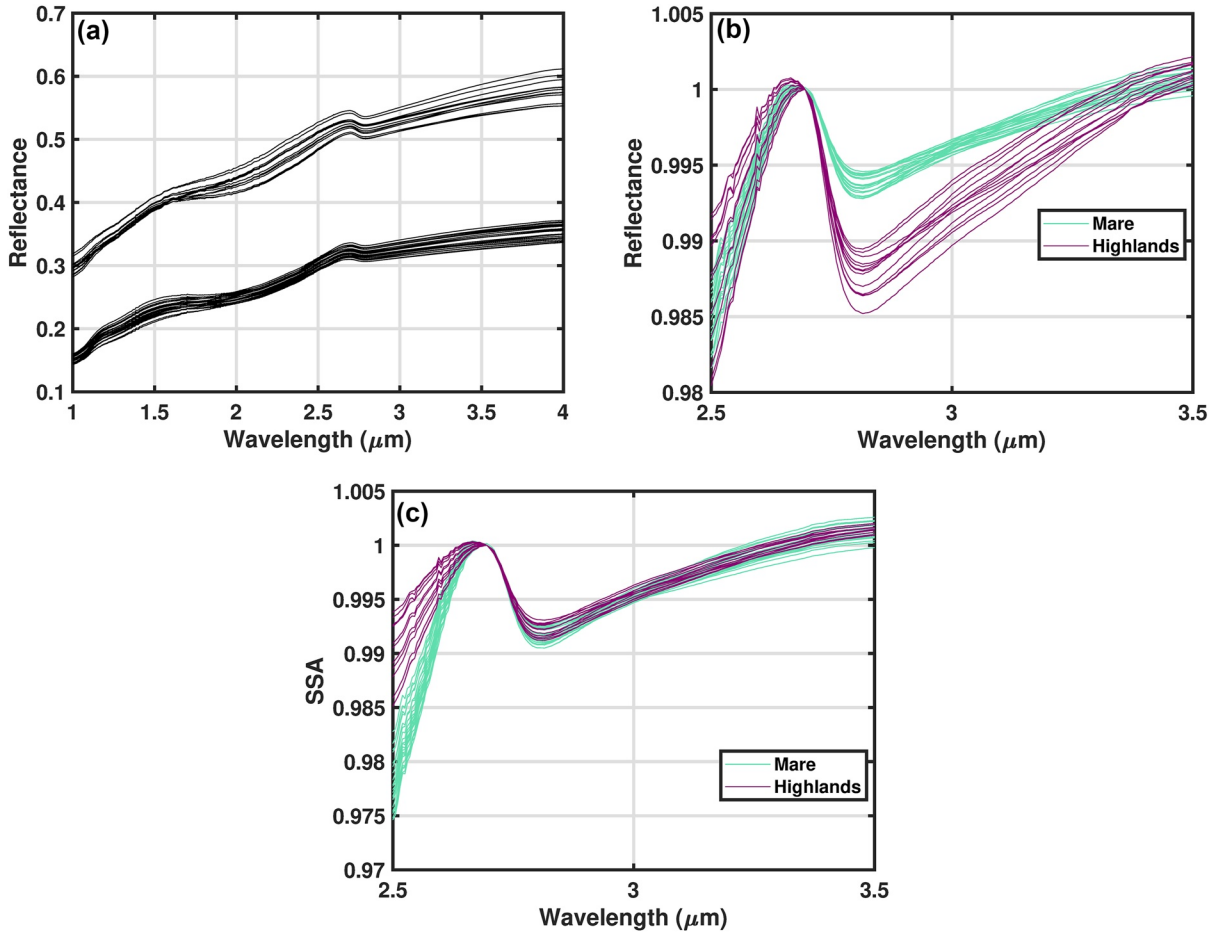

Figure 10. (a) Simulated mare and highlands noiseless spectra with total water abundances between 245 and 255 ppm. These lidar reflectance spectra are a subset of 36 of the 2000 simulated spectra. (b) Spectra from (a) after continuum removal using a convex-hull method. (c) Single scattering albedo spectra from which reflectance spectra in (a) and (b) were generated using Equation 1.

band depth results in a more sensitive measurement for the highlands simulations and a lower standard deviation for the simulations as a whole.

We found that the mean errors are all negative with a magnitude of between 14 ppm (yellow glass simulations) and 39 ppm (highlands simulations). We note that this is a statistical mean error over the 2,000 simulations, not a fixed error that applies uniformly to each retrieval. It does however indicate that there is a systematic error involved with our fitting methodology. The origin of this systematic error can be understood by looking at the total water errors plotted as a function of which interpolated MORB spectrum (see Figure 2) was mixed in to model the 3 μm absorption. This is shown in Figure 11a. Here it can be seen the largest negative errors were associated with higher values for the interpolated MORB spectrum used. In Figure 10b, we show a comparison of the interpolated MORB spectra used to generate the simulated spectra (black lines) to the experimental MORB spectra used for the retrieval (colored points). Figure 10c shows the residuals taken from subtracting the interpolated MORB spectra from the laboratory spectra. Evident from the residuals is a small band depth mismatch between the interpolated spectra (which assumes a perfect linear relationship between SSA and total water content) and the realistically non-linear experimental spectra from laboratory measurements (see Figure S7 in Supporting Information S1). Specifically, for the 1,522 ppm spectrum, the interpolated band shape is slightly shallower than the experimental band shape (negative residual). This band shape mismatch resulted in the least-squares algorithm fitting slightly too little of the laboratory 1,522 ppm endmember to the mixture and underestimating the total water content systematically.

This band shape mismatch is not an issue unique to our simulations but is always present to some extent when using library or laboratory spectra (or relationships generated from them such as linear ESPAT relationships) to

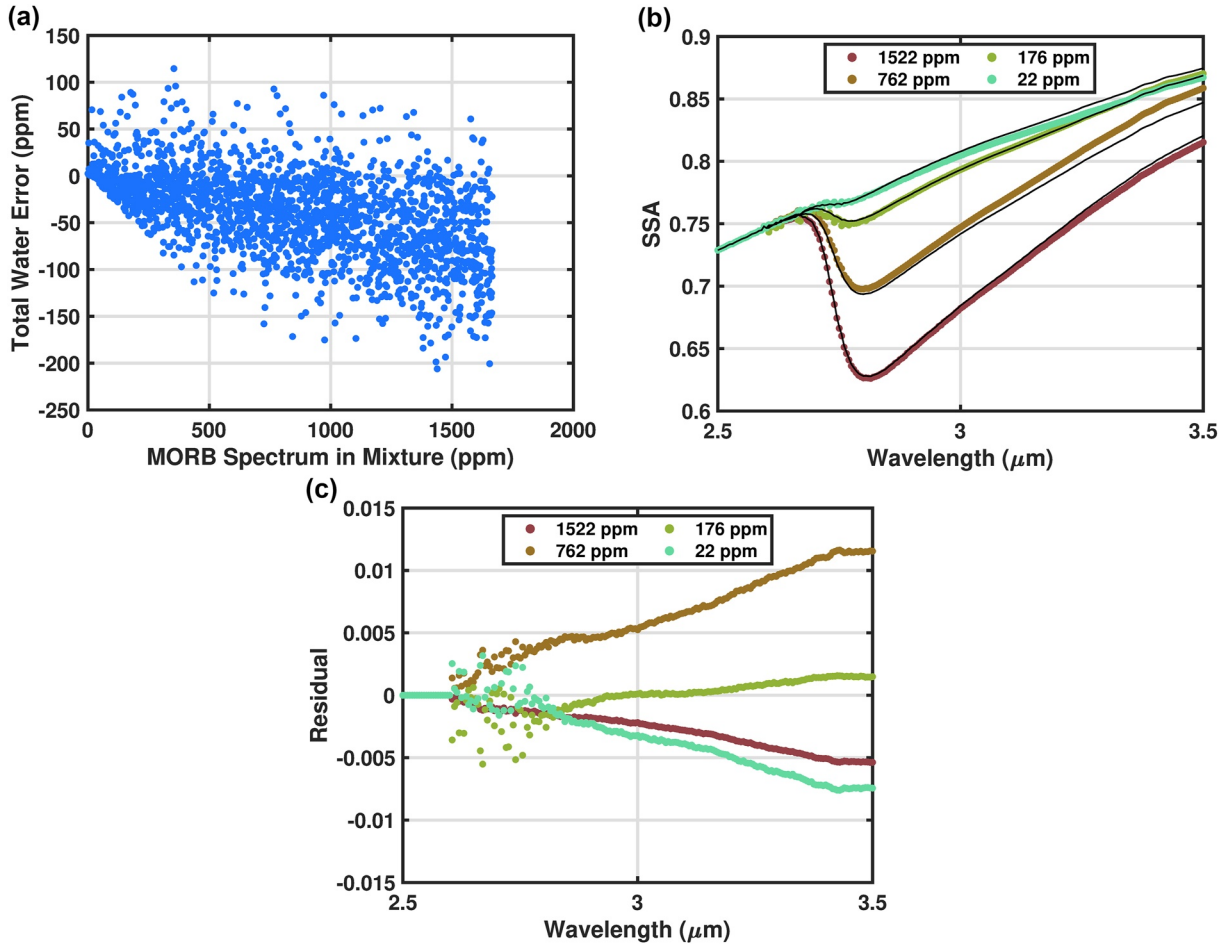

Figure 11. (a) Total water error as a function of input glass abundance and the interpolated MORB spectrum (Figure 2) used for each mixture. Each point corresponds to one spectrum/simulation. (b) Comparison of interpolated MORB spectra (obtained from a linear ESPAT fit) and laboratory MORB spectra at the same total water content for each. The total water content for each laboratory spectrum is given in the legend. (c) Residuals from (b) obtained from subtracting the interpolated MORB spectra from the laboratory MORB spectra for each experimental total water value.

fit remote sensing datasets (passively or actively obtained). In our case the "laboratory" spectra are the experimental MORB spectra, and the "remote sensing" spectra are the spectral mixtures using the interpolated MORB spectra (Figure 11b). This same phenomenon of band shape mismatch was observed with the synthetic lunar orange and yellow glass mixtures, where the differences between the MORB spectra used for fitting and the synthetic glass spectra used to create the mixture led to systematic errors in the retrievals on the order of 10s of ppm. The orange glass simulations exhibited a larger mean error than the yellow glass simulations, which is due to the band shapes of the synthetic glasses (Figure S8 in Supporting Information S1). The orange glass has a band minimum closer to 2.85 μm, while the yellow glass band minimum is near 2.8 μm, giving a better match to the MORB glass band minimum used for the retrieval.

We tested whether this systematic error was a function of the band shape difference (as described above) or the use of only these four wavelengths for the retrieval. We performed new retrievals on the orange and yellow glass spectra using the entire wavelength range between 1 and 4 μm for the least squares fitting procedure (approximating a passively obtained spectrum at 5 nm wavelength sampling). From these tests we found the band shape difference to be the primary cause of the systematic error. For the orange glass simulations, the mean error was still −53 ppm when using the entire wavelength range, the exact same as for the four-wavelength method. For the yellow glass simulations, the mean error was 0 ppm, an improvement of 11 ppm over the four-wavelength method.

When only considering the reflectance values at the lidar wavelengths the mare and highlands mixtures are quite similar in overall spectral shape, with the main differences coming from the absolute reflectance. The mean errors

and standard deviations for the two sets of simulations were very similar, differing by less than 5 ppm for the mean error and less than 15 ppm for the standard deviation. To convert the lidar measurement precision to band depth, we used the largest standard deviation of the retrieval error (52 ppm for the mare simulations) and created a new set of spectral mixtures all with 52 ppm total water (see supplementary material for details). Measured band depth depends on both the albedo of the regolith (as discussed above and shown in Figure 10) and how the continuum is defined. From these simulations 52 ppm of total water corresponded to a relative 2.8 μm band depth to a precision of 0.62% in *lidar* reflectance (Figure S10 in Supporting Information S1). Comparing this precision with the precision of passive spectrometer results is not straightforward, and even direct comparison between varying precision metrics present in the literature (ESPAT, band depth, integrated band depth, abundance) is difficult. However, this precision is generally in line with or slightly better than the band depth precision reported from M^3 results (S. Li & Milliken, 2017; McCord et al., 2011) and the ground-based IRTF (Honniball et al., 2020).

With the largest error of 52 ppm for the mare simulations, variations in the 3 μm band can be distinguished using this four wavelength lidar system. Taking the conservative side of recent observations, Honniball et al. (2020) report latitudinal and time of day variations of at least 100–200 ppm total water. Measurements with a lidar system as described here with a maximum error of 52 ppm would be able to distinguish these diurnal and latitude variations and make the first measurements of night-side hydration. If variations of any magnitude are observed, it refutes models and processes that lead to no variation of hydration on the lunar surface. This magnitude of error is also suitable to test the models of Jones et al. (2018) and Tucker et al. (2019) that show 60–100 ppm variations of total water with latitude or lunar local time. S. Li and Milliken (2017) performed analysis of M^3 data showing diurnal trends of several hundred ppm, which would be easily observable by this technique. Finally, Sunshine et al. (2009) observed changes in the 2.8 μm band depth of 3%–5%, which is achievable by our approach which can measure to sub-1% band depth precision. The distribution of total water on the surface of the Moon is of high importance when distinguishing between different formation, transport, and retention models. With a maximum error of 52 ppm, a lidar system can map the distribution of total water as a function of latitude and time of day to about the same precision as M^3 without any need to correct for surface temperature or observing geometry.

5. Conclusions

We have performed reflectance simulations for a multispectral lidar operating in the 3 μm band with the goal of assessing its ability to measure diurnal and latitudinal hydration variations on the lunar surface. We created spectral mixtures of highlands and mare soils and used hydrated MORB glass spectra to controllably introduce a total water signature similar to that observed from orbital and ground-based spectrometers. We then used a least-squares algorithm to solve for the endmember spectra and the total water abundance in each spectrum. The simulation results indicate that a four-wavelength multispectral lidar with laser wavelengths at 1.5 μm, 2.65 μm, 2.80 μm, and 3.1 μm could measure the hydration signature with a mean error between −10 and −39 ppm and a standard deviation of 52 ppm or less. Simulations of mixtures using hydrated synthetic lunar glasses confirmed that the mean error from the retrievals was a result of band shape mismatch between the observed and retrieved spectra and was not a result of using only four lidar wavelengths to sample the spectrum. The results from the synthetic lunar glass simulations suggest that measuring at multiple points within the 3 μm band helped reduce errors due to band shape mismatch. This 52-ppm precision, combined with the ability to measure over the entire diurnal cycle and at all locations with a fixed viewing geometry, suggests multispectral lidar observations in this wavelength regime would provide a valuable new remote sensing dataset. Constraining lunar hydration over the entire diurnal cycle at all latitudes would elucidate mechanisms of OH/H_2O generation, migration, and destruction crucial to understanding the lunar volatile cycle in the past, present, and future.

Data Availability Statement

The endmember reflectance spectra for the Apollo samples are available at the Keck/NASA Reflectance Experiment Laboratory managed by Brown University and hosted by the Planetary Data System Geosciences Node (https://pds-speclib.rsl.wustl.edu/). The specific spectra can be found by performing a keyword search and checking the box for "Include Specimen ID in search." The mature highlands spectrum can be found by searching for keyword "62231" and selecting the search result "LR-CMP-098." The immature highlands spectrum can be found by searching for keyword "61221" and selecting the search result "LR-CMP-106." The mature mare spectrum can

be found by searching for keyword "70181" and selecting the search result "LR-CMP-023." The immature mare spectrum can be found by searching for keyword "71061" and selecting the search result "LR-CMP-026." The pyroxene spectrum can be found by searching for keyword "15555" and selecting the search result "LR-CMP-168." The synthetic orange and yellow glass spectra can be found by searching for keywords "OGV-5" and "YG-5," respectively. The MORB glass reflectance spectra included in this paper are from Li (2016); Li and Milliken (2017) and Shimizu et al. (2016). The MATLAB code and endmember spectra (regolith and MORB) used to perform the simulations and analysis in this work are available at: https://doi.org/10.5281/zenodo.6025377 (Cremons, 2022).

Acknowledgments
This study is supported by NASA Goddard Space Flight Center and National Aeronautics and Space Administration. Dr. Honniball is also supported by an appointment to the NASA Postdoctoral Program at the NASA Goddard Space Flight Center administered by Oak Ridge Associated Universities under contract with NASA.

References

Abshire, J. B., Ramanathan, A. K., Riris, H., Allan, G. R., Sun, X., Hasselbrack, W. E., et al. (2018). Airborne measurements of CO_2 column concentrations made with a pulsed IPDA lidar using a multiple-wavelength-locked laser and HgCdTe APD detector. *Atmospheric Measurement Techniques*, *11*(4), 2001–2025. https://doi.org/10.5194/amt-11-2001-2018

Almeev, R., Holtz, F., Koepke, J., Haase, K., & Devey, C. (2008). Depths of partial crystallization of H_2O-bearing MORB: Phase equilibria simulations of basalts at the MAR near Ascension Island (7–11°S). *Journal of Petrology*, *49*(1), 25–45. https://doi.org/10.1093/PETROLOGY/EGM068

Bandfield, J. L., Poston, M. J., Klima, R. L., & Edwards, C. S. (2018). Widespread distribution of OH/H_2O on the lunar surface inferred from spectral data. *Nature Geoscience*, *11*(3), 173–177. https://doi.org/10.1038/s41561-018-0065-0

Bowell, E., Hapke, B., Domingue, D., Lumme, K., Peltoniemi, J., & Harris, A. (1989). Application of photometric models to asteroids. In *Asteroids II* (pp. 524–556). University of Arizona Press.

Burns, R. G. (1993). *Mineralogical applications of crystal field theory. Mineralogical applications of crystal field theory* (2nd ed.). Cambridge University Press. https://doi.org/10.1017/CBO9780511524899

Chai, M., Brown, J. M., & Slutsky, L. J. (1997). The elastic constants of an aluminous orthopyroxene to 12.5 GPa. *Journal of Geophysical Research*, *102*(B7), 14779–14785. https://doi.org/10.1029/97JB00893

Chauhan, P., Chauhan, M., Verma, P. A., Sharma, S., Bhattacharya, S., Dagar, A. K., et al. (2021). Unambiguous detection of OH and H_2O on the Moon from Chandrayaan-2 imaging infrared spectrometer reflectance data using 3 μm hydration feature. *Current Science*, *121*(3), 391–401. https://doi.org/10.18520/cs/v121/i3/391-401

Clark, R. N. (1979). Planetary reflectance measurements in the region of planetary thermal emission. *Icarus*, *40*(1), 94–103. https://doi.org/10.1016/0019-1035(79)90056-3

Clark, R. N. (2009). Detection of adsorbed water and hydroxyl on the Moon. *Science*, *326*(5952), 562–564. https://doi.org/10.1126/science.1178105

Cloutis, E. A. (2002). Pyroxene reflectance spectra: Minor absorption bands and effects of elemental substitutions. *Journal of Geophysical Research*, *107*(E6), 6–1. https://doi.org/10.1029/2001JE001590

Cohen, B. A., Hayne, P. O., Greenhagen, B., Paige, D. A., Seybold, C., & Baker, J. (2020). Lunar Flashlight: Illuminating the lunar South Pole. *IEEE Aerospace and Electronic Systems Magazine*, *35*(3), 46–52. https://doi.org/10.1109/MAES.2019.2950746

Cremons, D. R. (2022). Software for simulating lunar surface hydration measurements for multispectral Lidar at 3 μm (1.0.0). *Zenodo*. https://doi.org/10.5281/zenodo.6025377

Cremons, D. R., Abshire, J. B., Lucey, P. G., Stubbs, T. J., & Mazarico, E. (2020). Multiwavelength Lidar for remote spectroscopic measurements of the lunar surface. *Lunar Surface Science Workshop*, *2241*, 5068

Deutsch, A. N., Neumann, G. A., & Head, J. W. (2017). New evidence for surface water ice in small-scale cold traps and in three large craters at the north polar region of Mercury from the Mercury Laser Altimeter. *Geophysical Research Letters*, *44*(18), 9233–9241. https://doi.org/10.1002/2017GL074723

Dyar, M. D., Hibbitts, C. A., & Orlando, T. M. (2010). Mechanisms for incorporation of hydrogen in and on terrestrial planetary surfaces. *Icarus*, *208*(1), 425–437. https://doi.org/10.1016/j.icarus.2010.02.014

Farrell, W. M., Hurley, D. M., & Zimmerman, M. I. (2015). Solar wind implantation into lunar regolith: Hydrogen retention in a surface with defects. *Icarus*, *255*, 116–126. https://doi.org/10.1016/j.icarus.2014.09.014

Fisher, E. A., Lucey, P. G., Lemelin, M., Greenhagen, B. T., Siegler, M. A., Mazarico, E., et al. (2017). Evidence for surface water ice in the lunar polar regions using reflectance measurements from the lunar orbiter laser altimeter and temperature measurements from the diviner lunar radiometer experiment. *Icarus*, *292*, 74–85. https://doi.org/10.1016/j.icarus.2017.03.023

Gardner, C. S. (1982). Target signatures for laser altimeters: An analysis. *Applied Optics*, *21*(3), 448–453. https://doi.org/10.1364/ao.21.000448

Goguen, J. D., Stone, T. C., Kieffer, H. H., & Buratti, B. J. (2010). A new look at photometry of the Moon. *Icarus*, *208*(2), 548–557. https://doi.org/10.1016/j.icarus.2010.03.025

Green, R., Pieters, C., Mouroulis, P., Eastwood, M., Boardman, J., Glavich, T., et al. (2011). The Moon Mineralogy Mapper (M3) imaging spectrometer for lunar science: Instrument description, calibration, on-orbit measurements, science data calibration and on-orbit validation. *Journal of Geophysical Research*, *116*(E10). https://doi.org/10.1029/2011je003797

Grumpe, A., Wöhler, C., Berezhnoy, A. A., & Shevchenko, V. V. (2019). Time-of-day-dependent behavior of surficial lunar hydroxyl/water: Observations and modeling. *Icarus*, *321*, 486–507. https://doi.org/10.1016/j.icarus.2018.11.025

Hapke, B. (1986). Bidirectional reflectance spectroscopy: 4. The extinction coefficient and the opposition effect. *Icarus*, *67*(2), 264–280. https://doi.org/10.1016/0019-1035(86)90108-9

Hapke, B. (2012). *Theory of reflectance and emittance spectroscopy* (2nd ed.). Cambridge University Press.

Hendrix, A. R., Hurley, D. M., Farrell, W. M., Greenhagen, B. T., Hayne, P. O., Retherford, K. D., et al. (2019). Diurnally migrating lunar water: Evidence from ultraviolet data. *Geophysical Research Letters*, *46*(5), 2417–2424. https://doi.org/10.1029/2018GL081821

Honniball, C. I., Lucey, P. G., Ferrari-Wong, C. M., Flom, A., Li, S., Kaluna, H. M., & Takir, D. (2020). Telescopic observations of lunar hydration: Variations and abundance. *Journal of Geophysical Research: Planets*, *125*(9), e2020JE006484. https://doi.org/10.1029/2020JE006484

Hubbs, J. E., Sun, X., Abshire, J. B., Lauenstein, J.-M., Sullivan, W., & Beck, J. D. (2018). *Evaluation of space radiation effects on HgCdTe avalanche photodiode arrays for Lidar applications*. *Infrared technology and applications XLIV*. In G. F. Fulop, C. M. Hanson, P. R. Norton, B. F. Andresen, & J. L. Miller (Eds.) (Vol. 10624, p. 15). SPIE. https://doi.org/10.1117/12.2304601

Ichimura, A., Zent, A., Quinn, R., Sanchez, M., & Taylor, L. (2012). Hydroxyl (OH) production on airless planetary bodies: Evidence from H+/D+ ion-beam experiments. *Earth and Planetary Science Letters*, *345*, 90–94. https://doi.org/10.1016/j.epsl.2012.06.027

Jones, B. M., Aleksandrov, A., Hibbitts, K., Dyar, M., & Orlando, T. M. (2018). Solar wind-induced water cycle on the Moon. *Geophysical Research Letters*, *45*(20), 10–959. https://doi.org/10.1029/2018gl080008

Li, S. (2016). Water on the lunar surface as seen by the Moon minerology mapper: Distribution, abundance, and origins [PhD Thesis, Brown University]. https://doi.org/10.7301/Z0R49P73

Li, S., & Li, L. (2011). Radiative transfer modeling for quantifying lunar surface minerals, particle size, and submicroscopic metallic Fe. *Journal of Geophysical Research*, *116*(E9). https://doi.org/10.1029/2011je003837

Li, S., & Milliken, R. E. (2017). Water on the surface of the moon as seen by the moon Mineralogy Mapper: Distribution, abundance, and origins. *Science Advances*, *3*(9), e1701471. https://doi.org/10.1126/sciadv.1701471

Li, S. X., Yu, A. W., Sun, X., Fahey, M. E., Numata, K., & Krainak, M. A. (2017). A multi-wavelength IR laser for space applications. *Laser Radar Technology and Applications XXII*, *10191*, 101910L. https://doi.org/10.1117/12.2262391

Lucey, P. G. (1998). Model near-infrared optical constants of olivine and pyroxene as a function of iron content. *Journal of Geophysical Research*, *103*(E1), 1703–1713. https://doi.org/10.1029/97JE03145

Lucey, P. G., Neumann, G. A., Riner, M. A., Mazarico, E., Smith, D. E., Zuber, M. T., et al. (2014). The global albedo of the Moon at 1064 nm from LOLA. *Journal of Geophysical Research: Planets*, *119*(7), 1665–1679. https://doi.org/10.1002/2013JE004592

Lucey, P. G., Petro, N., Hurley, D., Farrell, W., Prem, P., Costello, E., et al. (2021). Volatile interactions with the lunar surface. *Geochemistry*, 125858. https://doi.org/10.1016/j.chemer.2021.125858

Mazarico, E., Neumann, G., Smith, D., Zuber, M., & Torrence, M. (2011). Illumination conditions of the lunar polar regions using LOLA topography. *Icarus*, *211*(2), 1066–1081. https://doi.org/10.1016/j.icarus.2010.10.030

McCord, T. B., Taylor, L. A., Combe, J.-P., Kramer, G., Pieters, C. M., Sunshine, J. M., & Clark, R. N. (2011). Sources and physical processes responsible for OH/H2O in the lunar soil as revealed by the Moon Mineralogy Mapper (M3). *Journal of Geophysical Research*, *116*(E6). https://doi.org/10.1029/2010JE003711

McKay, D. S., Heiken, G., Basu, A., Blanford, G., Simon, S., Reedy, R., et al. (1991). The lunar regolith. In *Lunar Sourcebook: A User's Guide to the Moon*. Cambridge University Press.

McLain, J. L., Loeffler, M. J., Farrell, W. M., Honniball, C. I., Keller, J. W., & Hudson, R. (2021). Hydroxylation of apollo 17 soil sample 78421 by solar wind protons. *Journal of Geophysical Research: Planets*, *126*(5), e2021JE006845. https://doi.org/10.1029/2021JE006845

Mustard, J. F., & Pieters, C. M. (1987). Quantitative abundance estimates from bidirectional reflectance measurements. *Journal of Geophysical Research*, *92*(B4), E617–E626. https://doi.org/10.1029/jb092ib04p0e617

Papike, J., Taylor, L., & Simon, S. (1991). Lunar minerals. *Lunar Sourcebook: A User's Guide to the Moon*, 121–181.

Pieters, C. M., Goswami, J. N., Clark, R. N., Annadurai, M., Boardman, J., Buratti, B., et al. (2009). Character and spatial distribution of OH/H_2O on the surface of the moon seen by M3 on Chandrayaan-1. *Science*, *326*(5952), 568–572. https://doi.org/10.1126/SCIENCE.1178658

Schaible, M. J., & Baragiola, R. A. (2014). Hydrogen implantation in silicates: The role of solar wind in SiOH bond formation on the surfaces of airless bodies in space. *Journal of Geophysical Research: Planets*, *119*(9), 2017–2028. https://doi.org/10.1002/2014JE004650

Schorghofer, N., Lucey, P., & Williams, J.-P. (2017). Theoretical time variability of mobile water on the Moon and its geographic pattern. *Icarus*, *298*, 111–116. https://doi.org/10.1016/j.icarus.2017.01.029

Shimizu, K., Saal, A. E., Myers, C. E., Nagle, A. N., Hauri, E. H., Forsyth, D. W., et al. (2016). Two-component mantle melting-mixing model for the generation of mid-ocean ridge basalts: Implications for the volatile content of the Pacific upper mantle. *Geochimica et Cosmochimica Acta*, *176*, 44–80. https://doi.org/10.1016/j.gca.2015.10.033

Smith, D. E., Zuber, M. T., Jackson, G. B., Cavanaugh, J. F., Neumann, G. A., Riris, H., et al. (2010). The lunar orbiter laser altimeter investigation on the lunar reconnaissance orbiter mission. *Space Science Reviews*, *150*(1–4), 209–241. https://doi.org/10.1007/s11214-009-9512-y

Starukhina, L. (2006). Polar regions of the moon as a potential repository of solar-wind-implanted gases. *Advances in Space Research*, *37*(1), 50–58. https://doi.org/10.1016/j.asr.2005.04.033

Starukhina, L., & Shkuratov, Y. G. (2010). Simulation of 3-μm absorption Band in lunar spectra: Water or solar wind Induced hydroxyl? 1385. Retrieved from https://ui.adsabs.harvard.edu/abs/2010LPI.41.1385S

Sun, X. (2017). *Lidar sensors from space*. In *Comprehensive remote sensing* (pp. 412–434). https://doi.org/10.1016/B978-0-12-409548-9.10327-6

Sun, X., Abshire, J. B., Krainak, M. A., Lu, W., Beck, J. D., Sullivan, W. W., et al. (2019). HgCdTe avalanche photodiode array detectors with single photon sensitivity and integrated detector cooler assemblies for space lidar applications. *Optical Engineering*, *58*(6), 067103. https://doi.org/10.1117/1.oe.58.6.067103

Sunshine, J. M., Farnham, T. L., Feaga, L. M., Groussin, O., Merlin, F., Milliken, R. E., & A'Hearn, M. F. (2009). Temporal and spatial variability of lunar hydration as observed by the Deep impact Spacecraft. *Science*, *326*(5952), 565–568. https://doi.org/10.1126/SCIENCE.1179788

Sunshine, J. M., & Pieters, C. M. (1993). Estimating modal abundances from the spectra of natural and laboratory pyroxene mixtures using the modified Gaussian model. *Journal of Geophysical Research*, *98*(E5), 9075–9087. https://doi.org/10.1029/93je00677

Taylor, L. A., Pieters, C., Patchen, A., Taylor, D.-H. S., Morris, R. V., Keller, L. P., & McKay, D. S. (2010). Mineralogical and chemical characterization of lunar highland soils: Insights into the space weathering of soils on airless bodies. *Journal of Geophysical Research*, *115*(E2). https://doi.org/10.1029/2009je003427

Taylor, L. A., Pieters, C. M., Keller, L. P., Morris, R. V., & McKay, D. S. (2001). Lunar mare soils: Space weathering and the major effects of surface-correlated nanophase Fe. *Journal of Geophysical Research*, *106*(E11), 27985–27999. https://doi.org/10.1029/2000je001402

Tucker, O. J., Farrell, W. M., Killen, R. M., & Hurley, D. M. (2019). Solar wind implantation into the lunar regolith: Monte Carlo simulations of H retention in a surface with defects and the H2 exosphere. *Journal of Geophysical Research: Planets*, *124*(2), 278–293. https://doi.org/10.1029/2018JE005805

Vasavada, A. R., Bandfield, J. L., Greenhagen, B. T., Hayne, P. O., Siegler, M. A., Williams, J.-P., & Paige, D. A. (2012). Lunar equatorial surface temperatures and regolith properties from the Diviner Lunar Radiometer Experiment. *Journal of Geophysical Research*, *117*(E12), a–n. https://doi.org/10.1029/2011JE003987

Warren, S. G., & Brandt, R. E. (2008). Optical constants of ice from the ultraviolet to the microwave: A revised compilation. *Journal of Geophysical Research*, *113*(D14). https://doi.org/10.1029/2007JD009744

Wetzel, D. T., Hauri, E. H., Saal, A. E., & Rutherford, M. J. (2015). Carbon content and degassing history of the lunar volcanic glasses. *Nature Geoscience*, *8*(10), 755–758. https://doi.org/10.1038/ngeo2511

Wöhler, C., Grumpe, A., Berezhnoy, A. A., & Shevchenko, V. V. (2017). Time-of-day–dependent global distribution of lunar surficial water/hydroxyl. *Science Advances*, *3*(9), e1701286.

Zuber, M. T., Head, J. W., Smith, D. E., Neumann, G. A., Mazarico, E., Torrence, M. H., et al. (2012). Constraints on the volatile distribution within Shackleton crater at the lunar South pole. *Nature*, *486*(7403), 378–381. https://doi.org/10.1038/nature11216